NONDESTRUCTIVE EVALUATION TECHNIQUES FOR SILICON CARBIDE HEAT-EXCHANGER TUBING

by

D.S. Kupperman, W.D. Deininger, N.P. Lapinski, C. Sciammarella and D. Vehas

Prepared for

ARPA/AFML Review of Progress in Quantitative NDE

La Jolla, California

July 8-13, 1979

ARGONNE NATIONAL LABORATORY, ARGONNE, ILLINOIS

Operated under Contract W-31-109-Eng-38 for the U. S. DEPARTMENT OF ENERGY

NONDESTRUCTIVE EVALUATION TECHNIQUES FOR SILICON CARBIDE HEAT-EXCHANGER TUBING*

D.S. Kupperman, W.D. Deininger, N.P. Lapinski, C. Sciammarella**, and D. Yuhas+
Materials Science Division, Argonne National Laboratory
Argonne, IL 60439

ABSTRACT

The adequacy of various nondestructive evaluation (NDE) techniques for inspecting silicon carbide heat-exchanger tubing is discussed. These methods include conventional ultrasonics, acoustic microscopy, conventional and dye-enhanced radiography, holographic interferometry and infrared scanning techniques. On the basis of current test results and an examination of the discussions in available literature, these techniques were compared with respect to (a) effectiveness in detecting cracks, pitting, inclusions, and voids, (b) effectiveness in characterizing detected flaws, (c) adaptability to tube geometry, (d) adaptability to in-service inspection, (e) reliability, and (f) extent of development required for commercialization.

INTRODUCTION

The production of reliable and long-lived structural ceramic components depends on the development of effective nondestructive evaluation (NDE) techniques. Since structural ceramics such as silicon carbide and silicon nitride have a critical flaw size an order of magnitude smaller than that of metals (e.g., on the order of 100 μm for silicon carbide), NDE methods that are adequate for metals may not be appropriate for ceramic materials. This paper describes an Argonne National Laboratory-Materials Science Division program to assess the effectiveness of various NDE methods applicable to silicon carbide heat-exchanger tubes, develop promising techniques, and establish a strategy for tube inspection. The techniques currently under evaluation include conventional ultrasonic testing, dye-enhanced radiograph, acoustic microscopy, infrared scanning (IR), and holographic interferometry. (The latter three techniques can also measure elastic properties, thermal conductivity and stress-intensity factors, respectively.) Techniques previously evaluated but no longer under study include acoustic impact testing, acoustic emission and internal friction. These techniques, although useful for evaluating the overall quality of components, have not been found practical for detecting very small defects. Overload proof testing has also been considered as an NDE method; however, this technique is very expensive and time-consuming and does not necessarily reproduce stresses encountered in the field environment. References 1-4 describe other techniques applicable to silicon carbide.

The tube specimens investigated in the present study were fabricated from siliconized, sintered and chemical-vapor-deposited (CVD) silicon carbide. (As will be shown later, the variation in microstructure among these three types of silicon carbide affects the sensitivity of ultrasonic inspection techniques. The tubes, obtained from Carborundum, Norton and Materials Technology Corporation (MTC), are approximately 1 m in length and 25 mm in diameter and have wall thicknesses ranging from 1 to 3 mm. The flaws sought were cracks, inclusions, voids and free silicon. Several of the techniques are discussed below and compared for effectiveness in detecting flaws.

DYE-ENHANCED RADIOGRAPHY

The dye-enhanced radiographic method is based on the filling of surface defects with a substance that will absorb penetrating radiation more effectively than the base material. Thus, surface defects, such as cracks and pitting, which are not generally revealed by ordinary radiography may become detectable when a dye is present. Dye enhancement has been most successfully used in conjunction with neutron radiography.[5] However, x-radiography is a more convenient technique. For x-radiography, the most effective doping agent found in the present investigation was a solution of silver nitrate and water (equal parts by weight). Figure 1 shows the ratio of mass absorption coefficients for silver nitrate and silicon nitride as a function of x-ray energy and wavelength. Silver nitrate absorbs x-rays approximately 20 times more strongly than silicon nitride; the ratio for silver nitrate and silicon carbide is similar. The absorption edge for silver results in a peak in the ratio of mass absorption coefficients at an energy of about 25 keV. The best contrast for silicon carbide was obtained at an x-ray energy of about 50 keV. The results obtained with a CVD silicon carbide tube approximately 1 mm thick, examined by radiography and subsequent metallographic sectioning, are typical. The largest crack (50 through the wall) found after sectioning was revealed by ordinary radiography, but four other cracks were revealed only by dye-enhanced radiography. Since good photographic reproductions of these radiographs were not obtainable, a similar result obtained from a cracked Plexiglass rod x-rayed with and without silver nitrate penetrant is shown in Fig. 2. The x-ray with the doping agent clearly shows numerous cracks that are not otherwise visible.

This technique has also been used to reveal dents in hot-pressed silicon carbide bars. For example, a dent ~ 25 μm and ~ 700 μm across was not indicated in conventional radiographs; however,

*Work supported by the U.S. Department of Energy

**Illinois Institute of Technology, Chicago, IL 60616
+Sonoscan, Inc., Bensenville, IL 60106

when filled with the silver nitrate doping agent, it was clearly seen by radiography.

HOLOGRAPHIC INTERFEROMETRY

The specific objective of the holographic interferometry effort is to assess the applicability of this technique to the detection of cracks in ceramic heat-exchanger tubing. Figure 3 shows a schematic representation of the optical system. Lens techniques are utilized to facilitate the application of double-beam holography and to allow for reconstruction with a less coherent source when a reduction of the speckle noise is needed.

1. Thermal Stress - The introduction of a temperature gradient can produce very high stresses on a tube. Heat-exchanger tubes were subjected to thermal gradients by means of a linear heating element located in the center of the tube, producing cracks. The outer-wall temperature was measured with a thermistor. Discontinuities in the interference pattern, produced by the cracks, were observed in real time and photographed. Examples are shown in Figs. 4 and 5. Figure 5 is particularly interesting because although the saw-cut crack is very shallow, the discontinuity produced by the presence of the crack is clearly visible in the fringe system.

2. Method for Obtaining the Stress-Intensity Factor from the Interference Pattern - No rigorous solution exists for a stress-intensity factor associated with a surface crack on a cylinder, which is subjected to a 3-D state of stress. However, an approximate solution may be derived as follows: If the v-displacement field is projected on a plane tangent to the cylinder, the displacement field parallel to the tube axis is given by

$$v = \frac{K_1}{G} \sqrt{\frac{r}{2\pi}} \, (2 - 2\nu) \sin\frac{\theta}{2} , \qquad (1)$$

where r is the distance from the crack tip, K_1 is the stress-intensity factor, G is the shear modulus, ν is Poisson's ratio, and θ is the angle with the tube axis. From the holographic moire pattern obtained by pressurizing the tube, we can obtain the displacement and the distance from the crack tip, and thus K_1. For example, if the displacement field is represented by Eq. 1, the fringe orders in the y-direction (perpendicular to the crack plane) should vary with $\sqrt{r}$; consequently, in a log-log plot, the fringe orders should plot as straight lines with a slope of 0.5. By inserting the appropriate values in Eq. 1, we obtain

$$v = 0.0243 \sqrt{r} \, K_1 \times 10^{-4} \qquad (2)$$

or

$$K_1 = \frac{41.09v}{\sqrt{r}} \times 10^4 . \qquad (3)$$

From a given order in the hologram, r and v are determined and thus K_1.

INFRARED SCANNING

This program evaluated the use of thermographic techniques to detect flaws and measure heat-transport properties in silicon carbide heat-exchanger tubing. In these investigations, the tubing (sprayed with graphite to ensure uniform emissivity) was heated at one end and simultaneously monitored with an IR camera to record temperature distributions due to axial heat flow. Computer modeling was used to help interpret the results, and thermocouples were placed on the silicon carbide tubes to establish the accuracy of quantitative IR scanning data.

1. Computer Modeling - A solution of the heat-conduction equation was used in a model for axial heat flow to aid in interpreting temperature-distribution data in silicon carbide tubing. Assume the tubes are finite rods of length L, and their initial temperature distribution is f(x). If there is no flow of heat at x = L, and the temperature (as a function of time) at x = 0 is $\phi_2(t)$, the temperature distribution along the tube is given by[6]

$$T(x,t) = \frac{2}{L} \sum_{n=0}^{\infty} e^{-t(\nu+\kappa\beta_n^2)} \cos(\beta_n x) \left\{ \kappa\beta_n(-1)^n \int_0^t e^{\lambda(\kappa\beta_n^2+\nu)} \phi_2(t)\,d\lambda + \int_0^L f(x') \cos(\beta_n x')\,dx' \right\} , \qquad (5)$$

where $\beta_n = (2n+1)\pi/2L$, $\kappa = K/\rho c$ (thermal diffusivity), $\nu = Hp/\rho cw$, room temperature is taken as the zero point, K is the thermal conductivity, p is the circumference, c is the specific heat, H is the coefficient of heat transfer, ρ is the density, and w is the cross-sectional area of the rod.

Assume the rod is initially at room temperature (therefore f(x) = 0 for all x), and after immersion of the end of the tube in a water bath, $\phi_2(t) = T_b$ (the bath temperature). Then for all $t \geq 0$, we get

$$T(x,t) = \frac{2}{L} \sum_{n=0}^{\infty} e^{-t(\nu+\kappa\beta_n^2)} \cos(\beta_n x) + \left\{ \kappa\beta_n(-1)^n \int_0^t T_b e^{(\kappa\beta^2+\nu)\lambda} d\lambda \right\} . \qquad (6)$$

After we evaluate the integral and simplify, the temperature distribution becomes

$$T(x,t) = \frac{2T_b}{L} \sum_{n=0}^{\infty} \frac{\kappa\beta_n(-1)^n}{\kappa\beta_n^2 + \nu} \cos(\beta_n x) \left[1 - e^{-t(\nu+\kappa\beta_n^2)} \right] . \qquad (7)$$

Equation (7) is valid for all t > 0 and for all x where 0 < x < L.

Two computer programs were written to evaluate Eq. (7). The first one calculated temperature vs position, along the rod as a function of time with various values of the thermal constants α and κ. The significant parameter was the thermal conductivity. As an example, when one end of the tube is at ~ 60°C, a 10% variation in the thermal conductivity results in a change in the tube temperature (as a function of position) of up to 1.5°C during heating and 0.8°C after equilibrium is reached at ~ 50°C. The curves allow prediction of Δt, the difference in temperature between equivalent points on two different rods. The other program calculated temperature vs time as a function of position along the rod for various thermal-conductivity values. Here again, with all other parameters unchanged, a 10% variation in the thermal conductivity resulted in a temperature variation of up to 1.5°C during heating and 0.8°C after equilibrium was reached. The experimental data may be compared directly with the calculated curves. A combination of the results allows the prediction of $\Delta T(\Delta x)$, the difference in temperature between two points on the same rod, as a function of time.

2. Experimental Measurements - Axial heat flow was examined in samples of silicon carbide heat-exchanger tubing to determine whether flaws in the tubes could be detected and to compare the thermal properties of different tubes. The experimental apparatus is shown in Fig. 6. Water flows into the basin and circulates freely to maintain a uniform temperature. A Styrofoam block holds the tubes in an upright position, with one end of each tube immersed in the water bath to a depth of ~ 3 cm. This allows simultaneous comparison of the temperature distributions produced by axial heat flow in several tubes. Data were obtained by making thermograms with an ACA Thermovision 750 IR camera, which is capable of resolving temperature differences of 0.2°C, and reading isotherm units from the color IR monitor. When quantitative measurements were made using the isotherm controls, a thermometer, with the mercury bulb sprayed with graphite, was heated with a heat gun to provide a reference temperature. Figure 7 shows a typical thermogram (initially in color) of the transient temperature distribution during axial heat flow. The different colors can be related to the surface temperature. As shown in Fig. 7, each tube had a unique heating rate. The temperature distribution in tube 4, which was severely cracked by thermal quenching, differs markedly from that of tube 3, which was not cracked. (Before tube 4 was cracked, the temperature distribution patterns in the two tubes were similar.) To examine the differential heating of the tubes more thoroughly, a series of thermograms were made with the tubes in different sequences. It was found that the Norton NC430 tubes always conducted heat better than the Carborundum Super KT tubes. To estimate the actual temperature differences between the tubes, ΔT (Δ tube), the scale on the left side of the thermogram in Fig. 7 was divided into 10 isotherm steps, each represented by a different color. The calibration curve for isotherm units vs temperature is linear in the 30-50°C temperature region. This implies that the color scale in the thermogram covers a 2°C temperature range. Analysis of Fig. 7 indicates that the NC430 tubes are ~ 1°C hotter at midheight than the KT tubes. According to data supplied by the manufacturers, the thermal conductivity of the NC430 tubing is 10% greater than that of KT. For tubes differing by this amount in thermal conductivity, Eq. (7) predicts an average temperature difference of 1°C during heating. Thus, the data are in reasonable agreement with the model prediction.

Three thermocouples were attached to tubes to obtain temperature-vs-time data at specific points along the tube. One thermocouple was attached to the top of the tube and the others [illegible] below the top using Hysol K20 conductive epoxy cement. Quantitative measurements made with the IR camera were compared with the thermocouple data as well as with the computer-model predictions to determine the adequacy of the IR camera in measuring temperature gradients. Figure [illegible] shows $\Delta T(\Delta X)$ for the top and middle thermocouples as a function of time. There was fair agreement between the computer-model predictions, the IR data, and the thermocouple data for elapsed times of 60 s. For example, the value of $\Delta T(\Delta X)$, as measured by thermocouples, is 3.6°C at 120 s. The IR data yield a value of 2.2°C and the computer model predicts a value of 3.3°C. However, as shown in Fig. [illegible], the IR scanning data show considerably smaller ΔT than the thermocouple and computer-model predictions. This can be attributed to human error in reading the calibration curve from the isotherm marker scale. The deviations from the model predictions for $t > 60$ s and $t > 250$ s are probably due to the inadequacy of approximating a solid rod with a small-diameter rod and the difficulty in accounting for convective cooling (i.e., in determining H).

INSPECTION OF SiC TUBES WITH AN ULTRASONIC IN-SIDE PROBE

Efforts are underway to develop a [illegible] ultrasonic probe for silicon carbide tubes. The conceptual design for the ultrasonic inspection of straight tubes is shown in Fig. [illegible]. A frequency higher than that conventionally used for metal tubes is chosen in order that flaws as small as ~ 100 μm can be resolved. The transducer is oriented parallel to the water-filled tube to generate waves axially down the tube. An acoustic mirror is placed below the probe to reflect the longitudinal beam to the wall for detection of wall thinning or delaminations. For crack detection, the angle of incidence is adjusted so that longitudinal waves incident on the inner surface are mode converted to shear waves traveling axially down the tube. The beam would have to be offset about 1 mm to generate circumferential shear waves. In all cases, a motor rotates the mirror so that a 360° scan can be made at each axial location. It is anticipated that the axial motion of the probe will be controlled by a microprocessor and stepping motor and that data on signal amplitude versus position in the tube will be stored and displayed via a computer. In Fig. 10, the resolution achievable by the scheme described above is shown for longitudinal waves. Figure 10a shows the radio-frequency inner-wall reflection and backwall echo seen when a 20-MHz, 1/8-in.-diameter probe is used from the bore side with a 45° reflector. An "impulse"-type initial pulse is used. With a "tuned" initial pulse (Fig. 10b) and a different pulser-receiver used in the video-output mode, many more echos can be seen. The latter scheme may be more sensitive than the former for locating defects. The evalu-

uation of these two systems is continuing.

Electric-discharge-machined reference notches were made in a sintered silicon carbide tube. The tube was radiographed to confirm the notch size and depth, and was then interrogated ultrasonically from the outside to estimate the sensitivity of this inspection method. A 20-MHz, 6-mm-dia transducer and Sonic Mark III pulser-receiver were employed. The large notches (50 x 250 μm deep) were clearly evident in the video mode; the smaller notches (25 x 125 μm) could also be resolved, but not as readily. Searching for the notches from the OD is hampered by the curvature of the tube, which results in a defocusing of the beam as it passes through the wall. When the tube is inspected ultrasonically from the bore side, however, the opposite occurs; the curvature tends to focus the beam.

ACOUSTIC MICROSCOPY

1. Effect of Microstructure - Several types of silicon carbide samples with different microstructures were investigated, employing through-transmission acoustic microscopy techniques. Hot-pressed, sintered, siliconized, and CVD samples were examined. The effect of the variation in microstructure on the acoustic-microscopy results is discussed below.

Two types of siliconized tubes (Norton NC430 and Carborundum KT) were electrolytically etched in the solution described in Ref. 7 to reveal the microstructural differences between them. Figure 11a shows an etched sample of CVD silicon carbide tubing supplied by MIT, with grains up to 50 μm in size and some porosity. The KT material (Fig. 11b) has small grains, with a maximum size of 25 μm. NC430 (Fig. 11c) has a bimodal distribution of grain sizes, with a maximum size of 100 μm. The light areas seen in both materials are free silicon. Figures 12a and b show optical micrographs of hot-pressed (Norton) and sintered (Carborundum) silicon carbide samples, respectively. Pores (dark areas), generally less than 10 μm in size, are more prevalent in the sintered material.

Acoustic micrographs of two siliconized silicon carbide tube samples (NC430 and SiT) and one CVD sample are shown in Fig. 13. The NC430 material (Fig. 13a) shows higher levels of acoustic noise than the smaller-grained SiT material (Fig. 13b), despite the fact that the SiT sample is thicker (3 vs 1 mm). The lines in the latter micrograph are curved because of the curvature of the sample. The 1-mm-thick CVD specimen (Fig. 13c) has a higher acoustic noise level than either siliconized specimen. Figure 14 shows acoustic micrographs of a 6-mm-thick bar of hot-pressed silicon carbide and a 1-mm-thick tube section of sintered silicon carbide. Although it is much thinner, the sintered specimen (Fig. 14b) is acoustically much noisier than the less porous hot-pressed specimen (Fig. 14a). However, the sintered specimen is less noisy than either of the siliconized samples (Figs. 13a and b). In summary, the hot-pressed SiC had the lowest level of acoustic noise of any of the materials examined and would be the easiest to inspect with through-transmission acoustic microscopy techniques, followed in increasing order of difficulty by the sintered, siliconized and CVD materials.

2. Defect Confirmation - This section discusses the localization, by destructive examination, of defects indicated by acoustic microscopy techniques. A piece of siliconized silicon carbide tubing (SiT), 25 mm in diameter with a 3-mm wall thickness, serves as an example. A flaw indication is evident in the acoustic micrograph of Fig. 15. Axial and radial radiographs of the intact tube section showed no flaw indications. The tube was cut down in size until an axial-view radiograph indicated a circumferential delamination about 1 mm across (in agreement with the acoustic-micrograph result) and approximately 0.3 mm below the surface. The sample was then ground down circumferentially to determine the axial length of the defect. Figure 16 shows the result. A delamination approximately 1.5 mm long was revealed, again in agreement with the acoustic-microscopy result.

As a result of the initial success in using the acoustic microscope to detect natural flaws in silicon carbide tube sections, a stage was developed to interface with the Sonoscan acoustic microscope so that a helical scan of a tube could be made. This stage is currently being evaluated.

COMPARISON OF TECHNIQUES

Clearly, there are many considerations in selecting an NDE technique for silicon carbide heat-exchanger tubes. One must consider the adaptability of the technique to the tube geometry, rate of inspection, applicability to in-service inspection, reliability, effectiveness of flaw detection and characterization and the development required for commercial use of the technique. Table I summarizes the results to date of the present investigation, in terms of these criteria. Table II gives the estimated sensitivities of some of the methods under ideal laboratory conditions. Among the techniques investigated, acoustic microscopy has been shown to be the most sensitive for detecting defects in silicon carbide tubing; this technique can also reveal the character of the defect. A surface defect of 100 μm long and 50 μm deep in a silicon carbide bar has been revealed by holographic interferometry techniques, using a 4-point bending fixture. The sensitivity of radiography has been improved through the use of dye-enhancement techniques. Infrared scanning has been shown to be useful for detecting variations in heat-transport properties, and conventional ultrasonic testing has been shown to be capable of detecting reflectors on the order of 100 μm in size using frequencies of 20 MHz or possibly higher, which are well above the frequencies normally used for metal tubes. At this time, the three most useful techniques for NDE of silicon carbide tubes appear to be acoustic microscopy, conventional ultrasonic testing from the bore side, and dye-enhanced radiography.

REFERENCES

1. A.G. Evans, G.S. Kino, P.T. Khuri-Yakub and B.R. Tittman, "Failure Prediction in Structural Ceramics," Mater. Eval. 35 (4), 85 (April 1977).

2. A.J. Bahr, "Microwave Techniques for Nondestructive Evaluation of Ceramics," Final Report AMMRC-CTR-77-29, SRI International, Menlo Park, CA (Nov. 1977).

3. B.T. Khuri-Yakub, "Acoustic Surface Wave Scattering: The Detection of Surface Cracks in Ceramics," Report SC5064-2TR, Rockwell International Science Center, Thousand Oaks, CA (Dec. 1977).

4. Y.H. Wong and R.L. Thomas, "Laser Photoacoustic Techniques for NDE," presented at the ARPA/AFML Review of Progress in Quantitative NDE, Scripps Institution of Oceanography, La Jolla, CA, July 17-21, 1978.

5. H. Berger, "Practical Applications of Neutron Radiography and Gauging," ASTM Special Technical Publication 586, American Society for Testing and Materials, Philadelphia (1975).

6. V.S. Arpaci, Conduction Heat Transfer, Addison/Wesley, Reading, MA (1966) p. 51.

7. G.W. Robinson and R.F. Gardner, "Ceramographic Preparation of Silicon Carbide," J. Am. Ceram. Soc. 47 (4) (April 1964).

Table I. Comparison of Several NDE Techniques for Flaw Detection in Silicon Carbide [illegible] or Tubing[a]

Method	Relative Effectiveness for Flaw Detection: Surface Cracks ID	Surface Cracks OD	Embedded Cracks ID	Embedded Cracks OD	Subsurface Inclusions	Voids	Effectiveness for Characterization of Defect Type	Adaptability to Automation	Adaptability to [illegible]	Adaptability to [illegible]	Equipment Cost	[illegible]	[illegible]
Acoustic Microscopy	G[b]	E	G	E	G/A	E	E	E	G	F	G/A	[illegible]	[illegible]
Dye-enhanced Radiography	G	G	G	G	[illegible]		G	G	E	P	G	[illegible]	[illegible]
Conventional Radiography	F	F	G	G	G	G	C	G	E	P	G	[illegible]	[illegible]
Conventional Ultrasonic Testing	G	G	G	G	G	G	F	F/G	E	[illegible]	G	[illegible]	[illegible]
Overload Proof Testing	G	G	?	?	?	?	P	P	P		F	[illegible]	[illegible]
Holographic Interferometry	?	G/A	F/A	F/P			E	E/G	G	F	F	very high	[illegible]
Infrared Scanning	P	P	P	P	P	P	P	E	E	G	G	[illegible]	[illegible]
	effective measure of heat transport properties												
Internal-friction Measurement	F	F	?	?	?	?	P	P	P	P	P	very high	slow
Fluorescent Dye Penetrant Testing	[illegible]	G	[illegible]	G	[illegible]	[illegible]	F	E	E	P	G/A	none	slow

[a] for tubes with wall thickness [illegible]

[b] E = excellent, G = good, F = fair, P = poor, [illegible] = not acceptable

Table II. Estimated Sensitivity of NDE Methods for Flaw Detection in Silicon Carbide Heat-exchanger Tubing

Technique	Smallest Anomalies Detectable
Acoustic Microscopy	Flaws $\leq$ 100 μm long
Holographic Interferometry	Flaws 100 μm long (with lens techniques)
Dye-enhanced Radiography	Surface flaws with depth = 0.5 % t
Infrared Scanning	2% variation in thermal conductivity
Conventional UT	Surface flaws ~ 100 μm deep

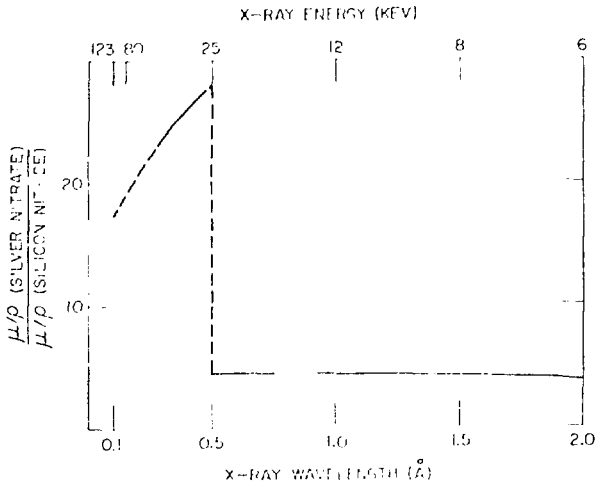

Fig. 1. Ratio of Mass Absorption Coefficients for Silver Nitrate and Silicon Nitride.

Fig. 2. Cracked Plexiglass Rod Radiographed Without and With Dye Enhancement.

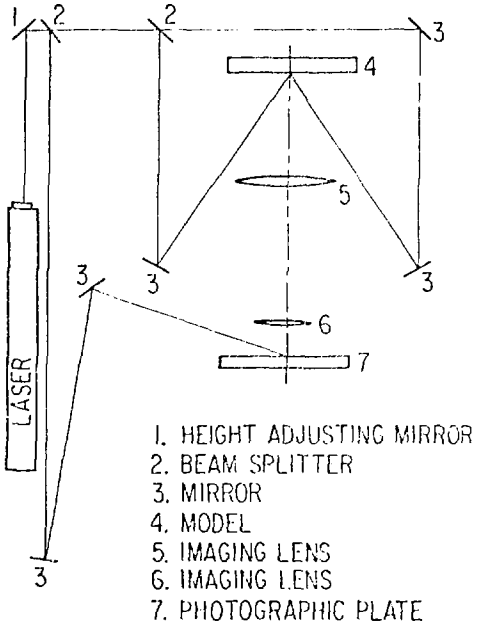

Fig. 3. Schematic Representation of Holographic Interferometry System.

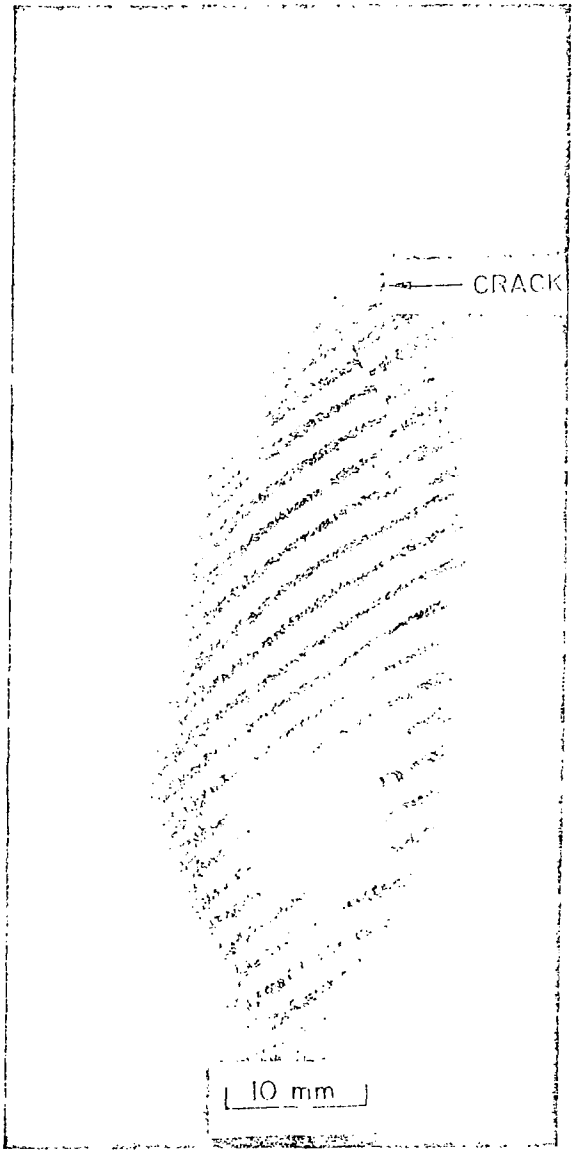

Fig. 4. Holographic Interferogram of Silicon Carbide Tube Showing Crack.

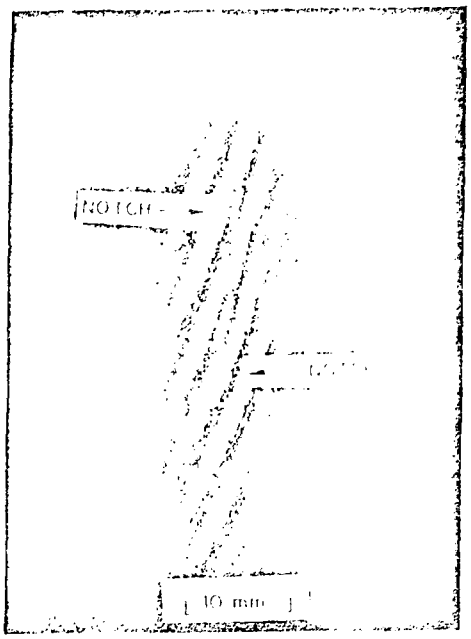

Fig. 5. Holographic Interferogram of Silicon Carbide Tube Showing Saw Cut (maximum depth 500 μm).

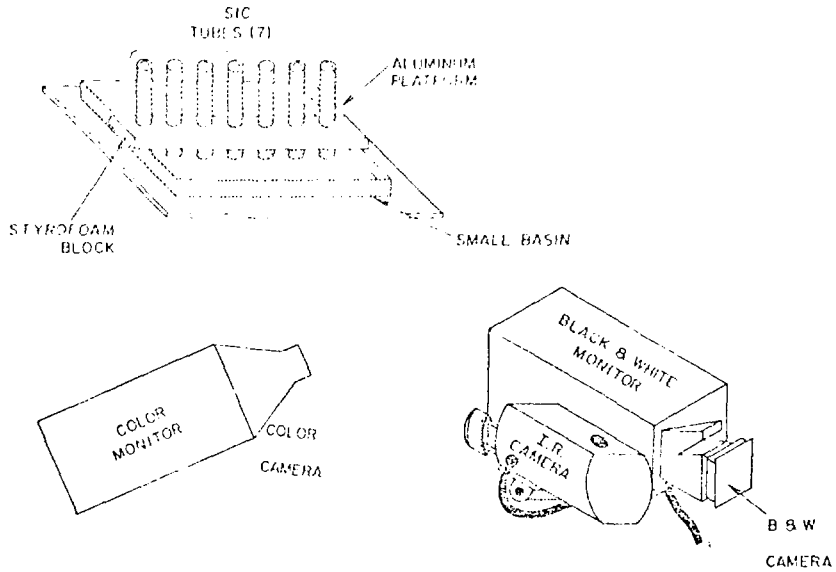

Fig. 6. Schematic of Infrared Scanning Apparatus

Fig. 7. Thermogram of Silicon Carbide Heat-exchanger Tubes. Tubes 1, 6 and 7 are Norton NC434; The others are Carborundum KT. Tube 4 was cracked by thermal quenching.

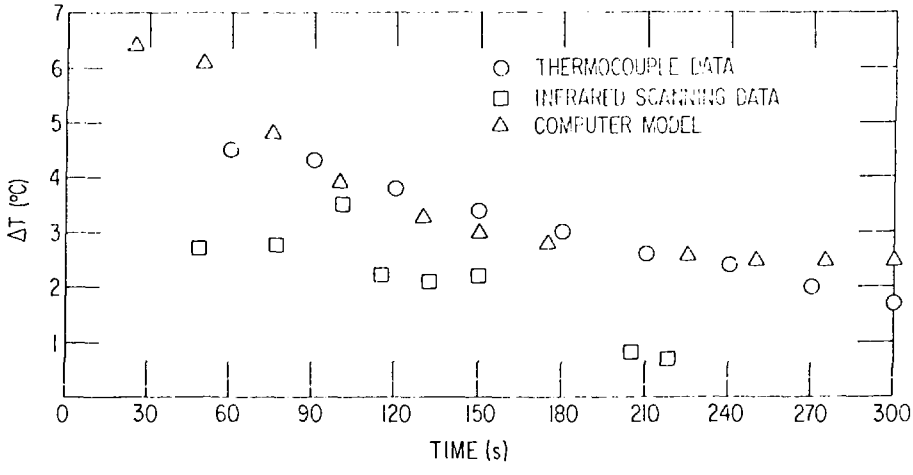

Fig. 8. Plot of $\Delta T(\Delta X)$ vs Time for Top and Middle Thermocouples, IR Data and Computer Model.

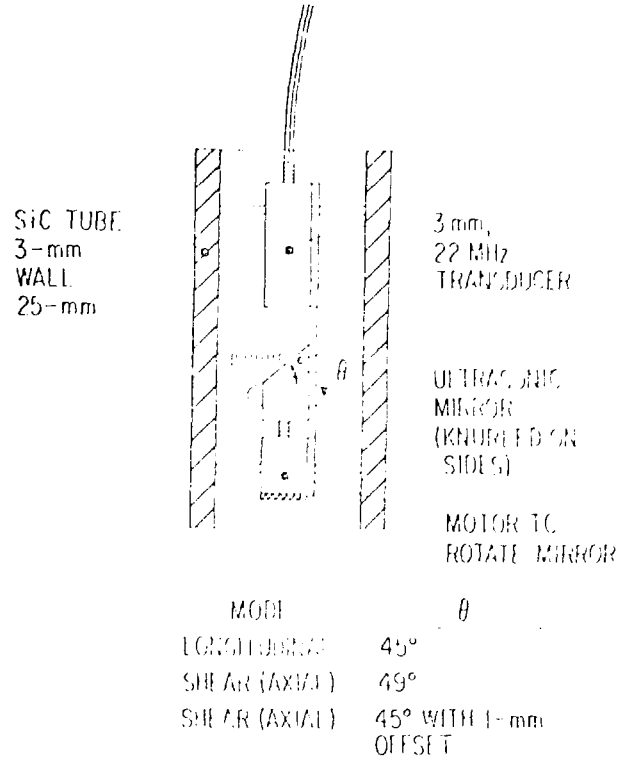

Fig. 9. Conceptual Design for Ultrasonic Bore-side Inspection of Silicon Carbide Tubes.

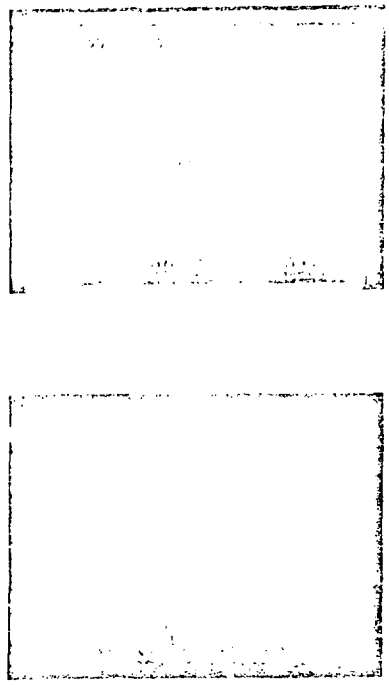

(a)

(b)

Fig. 10. Resolution of Normal-incidence Longitudinal Waves (20 MHz) from the Bore Side of a Silicon Carbide Tube with a 3-mm Wall Thickness. (a) Radio-frequency signal, (b) video output.

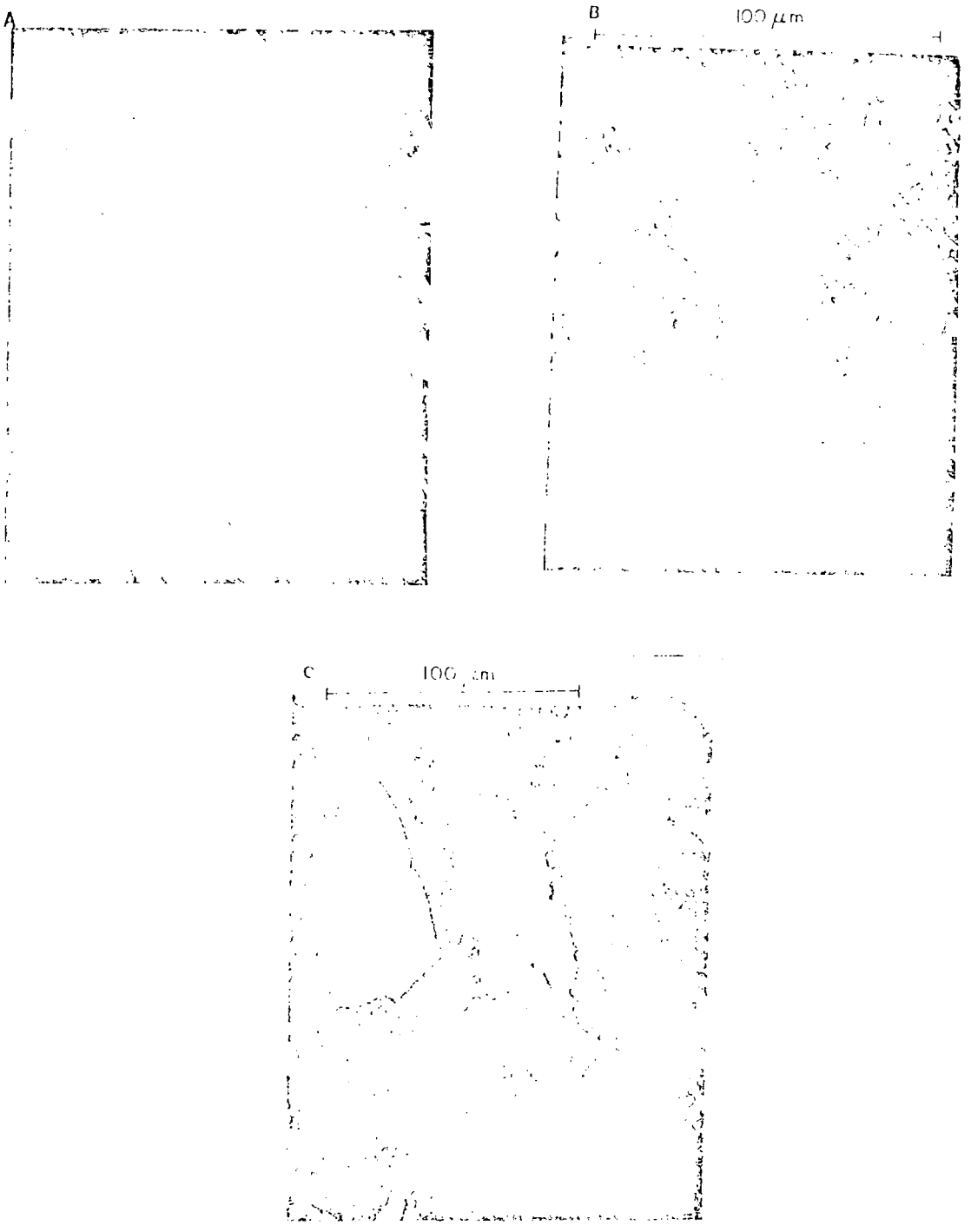

Fig. 11. Optical Micrographs of (a) CVD (Materials Technology Corporation), (b) Siliconized (Carborundum KT), and (c) Siliconized (Norton NC430) Silicon Carbide.

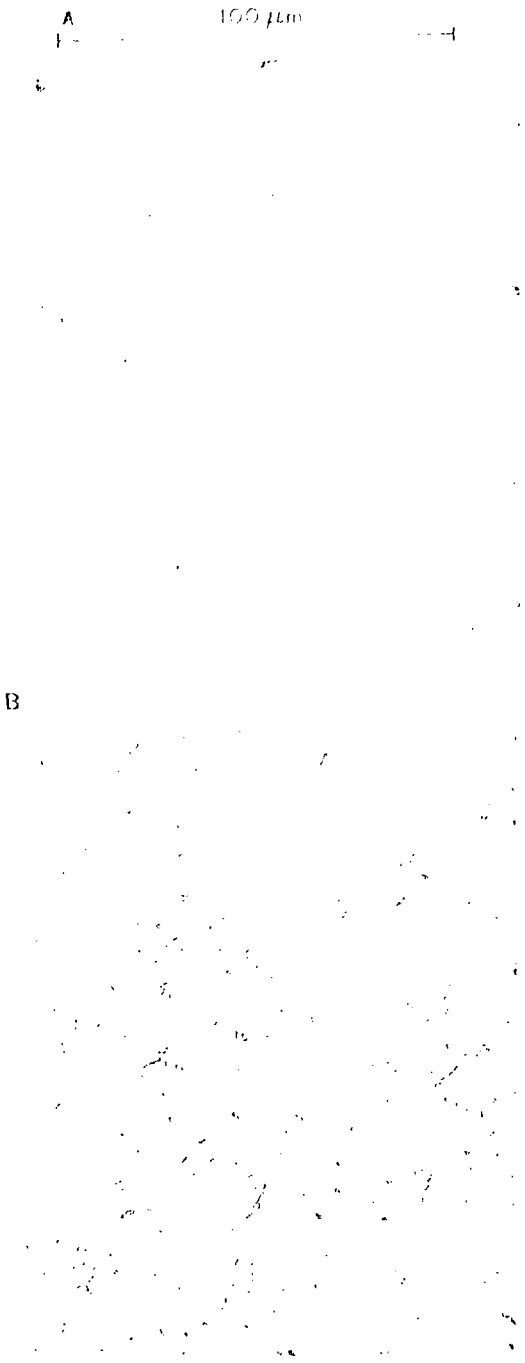

Fig. 12. Optical Micrographs of (a) Hot-pressed and (b) Sintered Silicon Carbide.

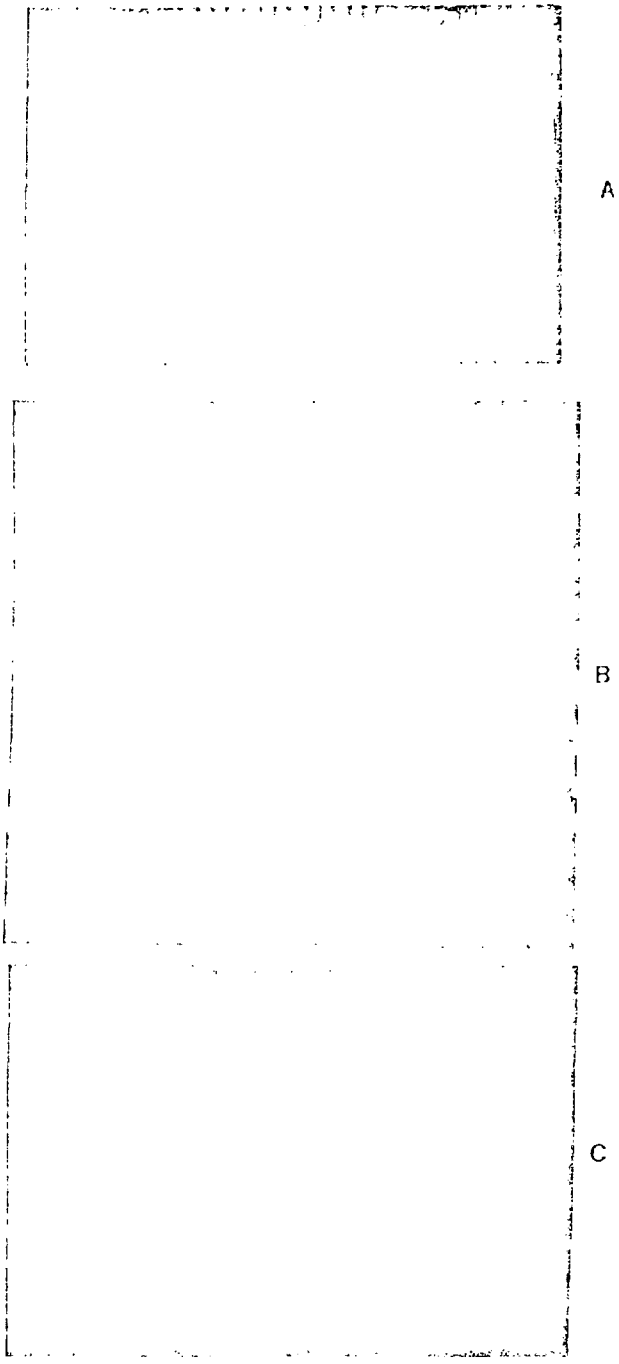

Fig. 13. Acoustic Micrographs of (a) Norton NC430, (b) Carborundum SKT, and (c) CVD Silicon Carbide.

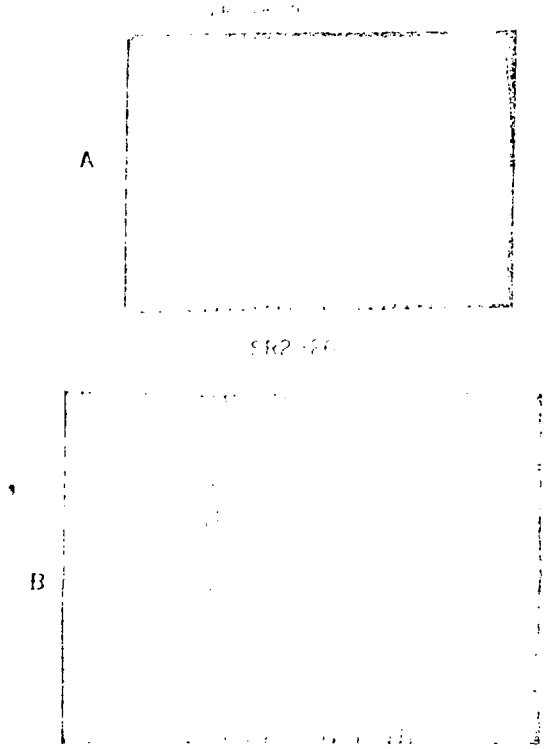

Fig. 14. Acoustic Micrographs of (a) Hot-pressed and (b) Sintered Silicon Carbide. Area shown is ~ 3 x 2 mm.

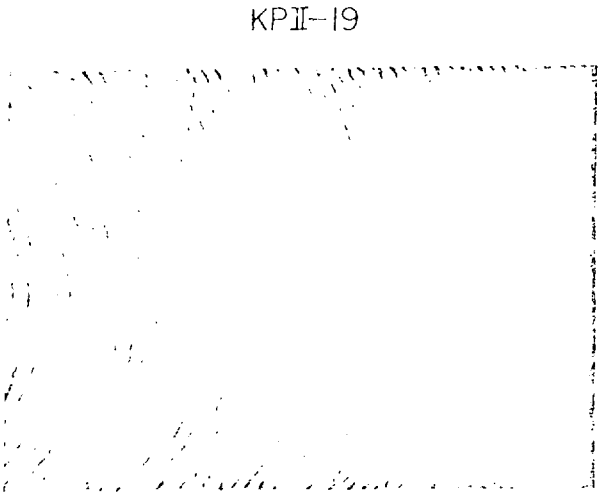

Fig. 15. Acoustic Micrograph of SiC Disc Showing Flaw. Area shown is ~ 3 x 2 mm.

Fig. 16. Destructive Examination Results Showing Defect Seen by Acoustic Microscopy in Fig. 15. Length of defect is ~ 1.5 mm.